RSC Advances

REVIEW

View Article Online
View Journal | View Issue

Cite this: *RSC Adv.*, 2022, **12**, 33641

Titanium dioxide-based anode materials for lithium-ion batteries: structure and synthesis

Huili Shi,[a] Chaoyun Shi,[a] Zhitong Jia,[a] Long Zhang,[a] Haifeng Wang[b] and Jingbo Chen *[ac]

Received 30th August 2022
Accepted 8th November 2022

DOI: 10.1039/d2ra05442f

rsc.li/rsc-advances

Lithium-ion batteries (LIBs) have high energy density, long life, good safety, and environmental friendliness, and have been widely used in large-scale energy storage and mobile electronic devices. As a cheap and non-toxic anode material for LIBs, titanium dioxide (TiO_2) has a good application prospect. However, its poor electrical conductivity leads to unsatisfactory electrochemical performance, which limits its large-scale application. In this review, the structure of three TiO_2 polymorphs which are widely investigated are briefly described, then the preparation and electrochemical performance of TiO_2 with different morphologies, such as nanoparticles, nanowires, nanotubes, and nanospheres, and the related research on the TiO_2 composite materials with carbon, silicon, and metal materials are discussed. Finally, the development trend of TiO_2-based anode materials for LIBs has been briefly prospected.

1 Introduction

The development of advanced energy conversion systems such as Lithium-ion batteries (LIBs) is an important way to alleviate the world's energy shortage and global warming problems. LIBs with high power density and high energy density used at electric vehicles, energy storage systems and smart grids are increasingly demanding,[1,2] but conventional LIBs are not sufficient to meet these demands, so new electrode materials with high capacity and low cost have become a hot research topic in recent years.[3] As the most successful anode material in commercial LIBs at present, graphite has several fatal problem. Firstly, the operating voltage of graphite is below 0.2 V *versus* Li/Li^+, which is close to the lithium deposition voltage. Lithium dendrites may be generated during the repeated charge and discharge process, resulting in internal short circuit and serious safety risks.[4] Compared with graphite, TiO_2 has a relatively high lithium insertion/extraction voltage of about 1.7 V, which can effectively avoid lithium dendrites. Secondly, the volume expansion of TiO_2 during charge and discharge (<4%) is much smaller than that of graphite (10%). However the theoretical capacity of TiO_2 is 335 mA h g^{-1}, which is similar to that of graphite (372 mA h g^{-1}).[5] Therefore, TiO_2 is one of the candidates materials to replace graphite for its excellent safety.[6,7] However, as a wide bandgap semiconductor material, TiO_2 has poor electronic conductivity (10^{-12} to 10^{-7} S cm^{-1}) and low Li^+ diffusion rate (10^{-15} to 10^{-9} cm^2 s^{-1}). To address these problems, current solutions are included: (1) Nanostructures designing to reduce ionic and electronic transport distances,[8] which facilitates the electron/ion transport by increasing the contact area of electrolyte/electrode material. (2) Composites designing to take advantages of the high conductivity of carbon and metal materials and the high capacity of silicon materials, which improves the overall conductivity of electron and lithium by the synergistic effect, thereby improving the electrochemical performance. In this paper, the structure and performance of TiO_2 are firstly briefly described, and then the research progress of TiO_2 nanostructures designing and composites designing which are two aspects to enhance the electrochemical performance are reviewed, and finally, the development trend of TiO_2 has further prospected.

2 Crystal structure and lithium storage mechanism of TiO_2

There are mainly three crystal types of TiO_2: anatase, rutile and brookite.[9] In addition, there are some rare crystal types, such as

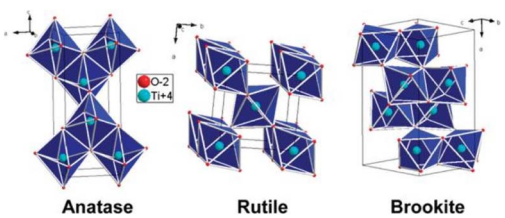

Fig. 1 Anatase, rutile, and brookite crystal structure of TiO_2.[10]

[a]*College of Chemistry and Chemical Engineering, Guizhou University, Guiyang, 550025, China*

[b]*College of Material and Metallurgy, Guizhou University, Guiyang, 550025, China*

[c]*Collaborative Innovation Center of Guizhou Province for Efficient Utilization of Phosphorus and Fluorine Resources, Guizhou University, Guiyang, 550025, China*

bronze. The crystal structures of anatase, rutile, and brookite are shown in Fig. 1.[10]

The basic composition of each crystal form is composed of an $[TiO_6]^{8-}$ octahedron included of one Ti^{4+} and six O^{2-}, and different connection modes and arrangement orders constitute different crystal structures of TiO_2. The anatase phase is composed of $[TiO_6]^{8-}$ octahedron with common edges, and its octahedra distortion is so significantly large that the symmetry is lower than that of the orthorhombic crystal system. The rutile phase is composed of $[TiO_6]^{8-}$ octahedrons with common tops and common edges, and its octahedral distortion is smaller than that of anatase, and its symmetry is better than that of anatase. The brookite phase belongs to the orthorhombic system, which consists of six TiO_2 to form a crystal cells. This crystal structure makes the brookite phase very unstable and therefore rare in nature. Table 1 lists the structure and lithium-storage properties of TiO_2 polymorphs. Generally speaking, the lithium insertion process of titanium dioxide can be expressed by eqn (1):

$$TiO_2 + xLi^+ + xe^- \rightarrow Li_xTiO_2 \quad (1)$$

The lithium insertion process of anatase TiO_2 can be divided into three regions (A, B, C) as shown in Fig. 2.[11]

Region A: The open-circuit voltage plunges to 1.8 V, and this region is considered as a small amount of Li^+ embedded in anatase lattice (Li_xTiO_2). In the bulk material, only 0.028 Li can be embedded, and reducing the particle size can increase the Li^+ accommodation capacity. The lithium embedding coefficients of large and small nanoparticles are up to 0.05 and 0.12.

Region B: A plateau appears around 1.75 V, a typical two-phase mechanism. Li^+ continues to be embedded in TiO_2 lattice, and the Li-poor phase of tetragonal crystal system changes to the Li-rich phase of orthogonal crystal system, and the two phases coexist. For bulk materials, the lithium content combined with the platform is 0.39 Li/TiO_2 formulation units.

Region C: The voltage decreases continuously and linearly below 1.7 V. The smaller the size of anatase crystal in this region, the larger the insertion amounts of Li^+.

The lithium-storage mechanism of other crystal types is rarely reported. The insertion of Li^+ in TiO_2 rutile is highly anisotropic, preferentially occurring in the *c*-axis,[12] tending to be one-dimensional, due to the large difference between the (*ab*-plane) *a*-axis and *c*-axis Li^+ diffusion coefficients. *c*-Axis pore channels are narrow, with a radius of 4 nm for octahedral

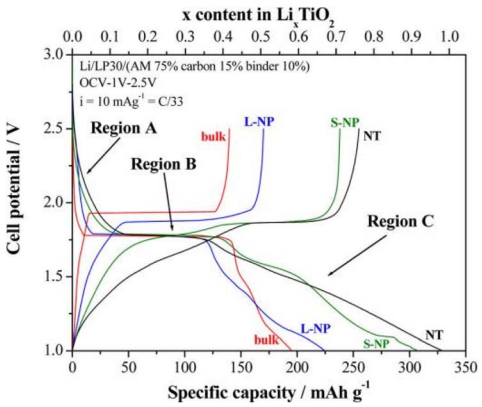

Fig. 2 The voltage–capacity curves of anatase TiO_2.[11]

vacancies and 6 nm for Li^+, so that only a small amount of Li^+ can be embedded at room temperature. With the insertion of Li^+, the diffusivity of Li^+ in rutile decreases, further limiting the embedding of Li^+. The process of Li^+ embedding brookite TiO_2 is also limited by structure, and the diffusion process is mainly along the direction of *c*-axis where the resistance is low. But the lithium storage mechanism is still unclear.

3 Pure nanostructured TiO_2 materials

TiO_2 materials have disadvantages such as low electrical conductivity, poor cycle performance and rate performance, however nanostructured TiO_2 electrode materials have the advantages of large surface area and short ion diffusion distance,[16] so the researchers are devoted to preparing various TiO_2 nanomaterials. In terms of dimensions, TiO_2 nanomaterials can be divided into zero-dimensional (TiO_2 nanoparticles[17,18]), one-dimensional (TiO_2 nanowires, TiO_2 nanorods, TiO_2 nanotubes, *etc.*[19–23]), two-dimensional (TiO_2 nanosheets[24–26]), three-dimensional (TiO_2 nanoflowers, TiO_2 nanospheres, TiO_2 nanotrees, *etc.*[27–29]). The studies find that the particle size, morphology, and surface area of nano-TiO_2 have obvious effects on its electrochemical performance. When the particle size decreases, TiO_2 nanomaterials have a larger active material/electrolyte contact area and shorter ion diffusion distance,[30] which can effectively improve the rate performance and high-current charge–discharge performance. The unique morphology can alleviate the volume expansion during lithiation/delithiation processes, and improve the cycle

Table 1 Structure and lithium-storage properties of TiO_2 polymorphs[13–15]

Polymorph	Crystal structure	Density (g cm^{-3})	Band gap energy (eV)	Unit cell (Å)	Li^+ insertion (mol)/ specific capacity (mA h g^{-1})	
					Bulk	Nano
Anatase	Tetragonal ($I4_1/amd$)	3.79	3.20–3.23	$a = 3.79$, $c = 9.51$	0.5/168	1.0/335
Rutile	Tetragonal ($P4_2/mnm$)	4.13	3.02–3.04	$a = 4.59$, $c = 2.96$	0.1/34	0.85/285
Brookite	Orthorhombic ($Pbca$)	3.99	3.14–3.31	$a = 9.17$, $b = 5.46$, $C = 5.14$	0.1/34	1.0/335

stability. The larger surface area can increase active material/electrolyte contact area, and thinner wall thickness can reduce the diffusion distance of Li^+, which is beneficial to improve the electrochemical performance.

3.1 Zero-dimensional TiO_2

TiO_2 nanoparticles. TiO_2 nanoparticle synthesis methods mainly include the sol–gel method,[31,32] hydrothermal method, template method, and microemulsion method. The size of TiO_2 nanoparticles is about 10–20 nm,[33,34] and their electrochemical performance is better than that of micron TiO_2 particles.[35] However, it is easy to agglomerate in the process of charging and discharging, which speeds up the capacity decay, and its cycle stability is poor.[36] The morphology of the material is a key factor affecting the electrochemical performance,[37] so the synthesis of TiO_2 nanoparticles is a feasible method to improve the performance of LIBs.

Partheeban *et al.*[38] used melamine as a soft template to prepare anatase phase TiO_2 nanoparticles with an average size of 10–20 nm. It showed excellent electrochemical performance with an initial discharge capacity of 272 mA h g^{-1} at 1C, a slight decrease of about 240 mA h g^{-1} after 50 cycles, and still had a capacity of 208 mA h g^{-1} after 1000 cycles. Zhang *et al.*[39] designed a two-step hydrothermal method for the preparation of brookite phase mesocrystalline TiO_2 using amorphous titanate as a precursor and oxalic acid as a structural guide (see Fig. 3), which maintained a capacity of 105.7 mA h g^{-1} after 500 cycles at 5C. Ouardi *et al.*[40] used titanium tetrisopropanol and sodium alginate as titanium precursor and template, respectively, and then calcined to prepare nano-sized TiO_2. At 0.1C, TiO_2 anode calcined at 300 °C and 450 °C had reversible capacities of 266 mA h g^{-1} and 275 mA h g^{-1} in the first cycle, respectively. Coulomb efficiencies are 70% and 75%, respectively. The cycling performances and capacities of TiO_2-nanoparticlesis depicted in Table 2.

3.2 One-dimensional TiO_2

TiO_2 nanowires. Compared with TiO_2 nanoparticles, TiO_2 nanowires exhibit some advantages such as stable and reversible capacity[41] and excellent rate performance. Common methods for the preparation of TiO_2 nanowires include the hydrothermal method, which can control the morphology and particle size by adjusting the solution concentration, titanium source, reaction temperature and reaction time, *etc.* The obtained products have better purity, controllable crystalline shape, uniform particles, and a simple operation process with low pollution.[42] In addition to the hydrothermal method, sol–gel method[43] and template method[44] are also commonly used.

Wang *et al.*[45] prepared TiO_2 nanowires containing anatase phase and a small amount of bronze phase by hydrothermal method with diameters of 40–80 nm and lengths of 400–1500 nm, and had a capacity of 280 mA h g^{-1} after 40 cycles at 140 mA g^{-1} with a coulombic efficiency close to 98%. Wu *et al.*[46] used the hydrothermal method to prepare anatase TiO_2 nanowires with initial discharge/charge capacities of 260 mA h g^{-1} and 224 mA h g^{-1} at 20 mA g^{-1}, respectively, and the reversible capacity remained around 216 mA h g^{-1} in the 20th cycle. At a current density of 200 mA g^{-1}, the discharge capacity was about 159 mA h g^{-1} at the 20th cycle, which showed good cycling stability. Wang *et al.*[47] synthesized porous linear TiO_2. And the synthesis process consisted of two steps, firstly, the synthesis of titanium ethanoate precursor nanowires by microwave-assisted solvothermal method, followed by the conversion of titanium ethanoate nanowires into porous TiO_2 nanowires with diameters of about 0.4–2 μm and lengths of 2–20 μm, having a high surface area of 252 m^2 g^{-1}. Its unique nanoporous structure results in better electrolyte permeability and faster diffusion rates of electrons and Li^+, as well as better buffering volume changes during charge/discharge cycles. The cycling performances and capacities of TiO_2 nanowires is depicted in Table 3.

TiO_2 nanorods. TiO_2 with cone, strip, shuttle, dumbbell, and rod shapes are generally referred to as TiO_2 nanorods in a broad sense. TiO_2 nanorods are mainly prepared by solvothermal and hydrothermal methods,[48–51] and their microscopic morphology is affected by the reaction temperature and reaction time, and an appropriate increase in reaction temperature is beneficial to the orientation and alignment of nanorods. In LIBs, shorter and finer nanorods are beneficial for the diffusion and transport of Li^+.

Seisenbaeva *et al.*[52] prepared anatase phase nanorods, using a one-step hydrothermal method. It had homogeneous mesopores, high porosity, a surface area of about 300 m^2 g^{-1}, and initial charge/discharge capacities of 299 mA h g^{-1} and 225 mA h g^{-1} at C/15, respectively. Ji[53] sintered titanium foil coated with sodium hydroxide solution at 800 °C to prepare TiO_2 nanorods, which mainly consisted of rutile phase, with a width of about 500 nm and a thickness of about 5 μm. At the same time, they also studied the effect of different temperatures on TiO_2 nanorods. Santhi *et al.*[54] used a hydrothermal method to synthesize TiO_2 nanorods at different pH value and it was showed that when pH = 7, the length of nanorods was about 300–350 nm and the diameter was about 70–100 nm. When the pH was

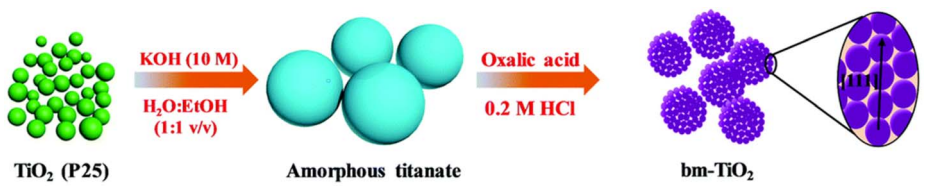

Fig. 3 Preparation process of mesomorphic TiO_2 with brookite phase.[39]

Table 2 Cycling performances and capacities of TiO_2 nanoparticles[a]

P_m	C_d	Initial coulombic efficiency	I_{dc}/mA h g^{-1}	C_n	R_c/mA h g^{-1}	Areal capacities (mA h cm^{-2})	Ref.
T_m	1C	50%	272	50	240	0.41	38
H_m	5C	58%	—	500	105.7	0.13	39
T_m	0.1C	75%	364	100	180	—	40

[a] P_m—preparation method, T_m—template method, H_m—hydrothermal method, C_d—current density, I_{ce}—initial coulombic efficiency, I_{dc}—initial discharge capacity, C_n—cycle numbers, R_c—remaining capacity, A_c—areal capacities.

Table 3 Cycling performances and capacities of TiO_2 nanowires[a]

P_m	L/nm	D/nm	C_d	C_n	R_c/mA h g^{-1}	Ref.
H_m	400–1500	40–80	140 mA g^{-1}	40	280	45
H_m	250	20	200 mA g^{-1}	20	159	46
S_m	2000–20 000	400–2000	0.2C	51	114.4	47

[a] P_m—preparation method, H_m—hydrothermal method, S_m—solvothermal method, L—length, D—diameter, C_d—current density, C_n—cycle numbers, R_c—remaining capacity.

increased to 9, the morphology was changed from rod-like structure to a platelet-like nanostructure.

TiO_2 nanotubes. TiO_2 nanotubes have a hollow structure that better satisfies the requirements for high surface area and relatively short conductive paths.[55,56] The main preparation methods are microwave, hydrothermal synthesis,[57] template, and anodic oxidation,[58] among which the anodic oxidation method is simple and easy to operate.[59]

Gong *et al.*[60] used the anodic oxidation method to prepare TiO_2 nanotubes with different diameters and lengths, and TiO_2 nanotubes arrays with diameters ranging from 30 nm to 90 nm could be obtained by controlling the anodic oxidation voltage. Xu *et al.*[61] used the hydrothermal method to prepare anatase TiO_2 nanotubes with a diameter of about 10 nm and a length about 200–400 nm. At 36 mA g^{-1}, the first charge–discharge capacities were 290 mA h g^{-1} and 238 mA h g^{-1}, respectively. At the 20th cycle, the reversible capacity was still about 200 mA h g^{-1}, and the coulomb efficiency is about 98%. Fasakin *et al.*[62] obtained TiO_2 nanotubes with average length, thickness, and diameter of 4 μm, 17 nm, and 20 nm, respectively. After stirring and hydrothermal treatment, the surface area of TiO_2 nanoparticles increased from the original 8 m^2 g^{-1} to 62 m^2 g^{-1}. The initial capacity of the original TiO_2 nanoparticles at a current density of 36 mA g^{-1} was 98 mA h g^{-1}, which decreased to 38 mA h g^{-1} at the 100th cycle. While the TiO_2 nanotubes showed an initial capacity of about 123 mA h g^{-1} at a current density of 36 mA g^{-1} and showed a capacity of 142 mA h g^{-1} at the 100th cycle, which increased by about 17% relative to the initial value. The cycling performances and capacities of TiO_2-nanotubes is depicted in Table 4.

TiO_2 nanofibers. Nanofibers are representative one-dimensional wire-like nanomaterials due to their high aspect ratio that have nanoscale diameter and large length, fast charge transfer and large specific surface area. Nanofibers can provide a continuous transport path to promote charge transfer and ion diffusion, reduce charge transfer resistance, and greatly improve electrode kinetics. At the same time, the high specific surface area of nanofibers can provide a large reaction contact area and a large number of active sites.[66] One-dimensional nanofibers are prepared by hydrothermal or solvent thermal synthesis,[67] chemical vapor deposition,[68] and electrostatic spinning.[69–71] Among them, electrostatic spinning method is most commonly used, simple and easy to achieve mass production.[72–74] Porous and continuous titanium dioxide nanofibers with large specific surface area can be prepared by the method. And the diameter, length and surface morphology of nanofibers can be controlled by adjusting the parameters of electrospinning process.

Zhuang *et al.*[75] synthesized TiO_2–B nanofibers with a specific surface area of 112 m^2 g^{-1}, high thermal stability and high crystallinity by steam thermal method. The initial capacity was 193.8 mA g^{-1}, which dropped to 189.5 mA g^{-1} after 100 cycles at 1C, with a good capacity retention rate of 97.8%. Luo *et al.*[76] synthesized unique MoO_2-modified TiO_2 nanofibers by electrospinning and layer-by-layer (LBL) self-assembly processes. It consisted of a TiO_2 nanofiber core and a thin metal-like MoO_2 nanolayer. MoO_2-modified TiO_2 nanofibers showed 514.5 mA h g^{-1} after 50 cycles at 0.2C. Zhu *et al.*[77] used electrospinning and sintering processes to prepare nanofibers, which showed stable performance at the end of 800 cycles at 150 mA g^{-1}, with a capacity retention of about 136 mA h g^{-1}.

3.3 Two-dimensional TiO_2

TiO_2 nanosheets. TiO_2 nanosheets[78] have a larger surface area, larger electrode/electrolyte contact area, and shorter Li^+ and electron transport paths. Compared with nanoparticles, it shows higher reversible charge/discharge capacity, better rate performance, and excellent cycling stability. And compared to mesoporous sphere, it shows shorter Li^+ diffusion paths. It has been synthesized by magnetron sputtering, multiple spin coating, sol–gel, and hydrothermal methods.[79,80]

Liu *et al.*[81] synthesized nanosheet-structured porous TiO_2 with a thickness of 5–10 nm by the solvothermal method, with an initial discharge capacity of 216 mA h g^{-1} at a high current density of 10C and maintained at 200 mA h g^{-1} after 200 cycles with a capacity retention rate of 92.6%. Wang *et al.*[82] used the multiple spin-coating methods on a fluorine-doped tin oxide substrate to prepare TiO_2 nanosheets arrays. More importantly, the size and shape can be controlled and the nanosheets arrays can be arranged on the substrate in an orderly and horizontally

Table 4 Cycling performances and capacities of TiO_2 nanotubes[a]

P_m	T/nm	C_d	Initial coulombic efficiency	C_n	R_c/mA h g^{-1}	Areal capacities (mA h cm^{-2})	Ref.
H_m	—	36 mA g^{-1}	82%	20	200	0.44	61
H_m	17	36 mA g^{-1}	94%	100	142	0.497	62
T_m	40	1C	72.2%	500	150	3.58	63
A_{om}	17	320 mA g^{-1}	—	50	179	—	64
H_m	3–4.5	0.1C	65%	50	265	1.33	65

[a] P_m—preparation method, H_m—hydrothermal method, T_m—template method, A_{om}—anodic oxidation method, T—thickness, C_d—current density, I_{ce}—initial coulombic efficiency, C_n—cycle numbers, R_c—remaining capacity, A_c—areal capacities.

homogeneous manner. Dai *et al.*[83] successfully prepared ultrathin TiO_2 nanosheets with a large surface area and fast electron transfer using a hydrothermal method with P123 as a soft template.

3.4 Three-dimensional TiO_2

TiO_2 nanoflowers. TiO_2 nanoflowers are nanomaterials with unique morphology and flower-like structure, which are of interest because of simple preparation, high surface area, and large porosity, and the three-dimensional structure has faster charge transfer capability and faster reaction rate on the surface. TiO_2 nanoflowers are synthesized by hydrothermal and precipitation methods, which are simple, non-toxic, and cost-effective, but the morphology of nanoflowers is difficult to control.[84]

Zhang *et al.*[85] synthesized homogeneous and hierarchical flower-like morphologies of TiO_2 with a diameter of 124 ± 5 nm by solvothermal method followed by hydrogenation. And the petals of TiO_2 nanoflowers consisted of nanosheets with a thickness of 10 ± 1.2 nm. After hydrogen reduction, Ti^{3+} or oxygen vacancies were introduced into the TiO_2 nanoflowers structure. The hydrogenated TiO_2 nanoflowers exhibited high capacity, excellent rate performance, and better cycling stability, with an initial discharge capacity of 179.6 mA h g^{-1} and the 200th discharge capacity of 177.1 mA h g^{-1} at 10C, with a capacity retention rate of 98.4% after 200 cycles. While the unhydrogenated TiO_2 nanoflowers presented an initial capacity of 130.1 mA h g^{-1} at a high current density, which decreased to 121.4 mA h g^{-1} after 200 cycles with a capacity retention rate of 93.4%. Pavasupree *et al.*[86] hydrothermally synthesized flower-like TiO_2 with a mesoporous structure. And it was composed of slightly curved nanosheets with a width of about 50–100 nm and a thickness of a few nanometers (see Fig. 4). The average pore size of TiO_2 nanosheets was about 3–4 nm, and the BET surface area and pore volume were about 642 m^2 g^{-1} and 0.774 cm^3 g^{-1}, respectively. Gao *et al.*[87] synthesized TiO_2 nanoflowers by a hydrothermal synthesis route in saturated sodium chloride solution.

TiO_2 hollow spheres. TiO_2 hollow spheres have good surface permeability, easily adjustable diameter and shell thickness.[88] Hollow structure alleviates the volume change during the insertion/extraction of Li^+, and increases the contact area of active material/electrolyte, effectively improving the transport rate of Li^+ and electrons in the electrode.[89–91] The template method is considered as a representative method of preparing hollow structures. It is grown on the template to form a core–shell structure, and then the template is removed. However, the template method faces some challenges, such as difficult to obtain uniform coatings due to compatibility issues between template and shell materials.[92,93] And template-free, solvothermal[94] (see Fig. 5), and sol–gel methods[95] are commonly used for the synthesis of TiO_2 hollow spheres.

Zhen *et al.*[89] synthesized hollow mesoporous TiO_2 microspheres by a template-free method. It had diameters of about 200–300 nm, mesopore diameters of about 12 nm, microspheres walls of about 200 nm, surface area of 105 m^2 g^{-1}, the first discharge capacity of about 215 mA h g^{-1} at 2C, and a capacity of 132 mA h g^{-1} at 2C after 200 cycles. In addition, it also exhibited excellent cycling stability, with the capacity retention of 100 mA h g^{-1} at 5C after 800 cycles. Yue *et al.*[96] synthesized mesoporous TiO_2 microspheres by solvothermal method, and the TiO_2 microspheres consisted of 6–8 nm nanocrystals with a uniform distribution of 4–8 nm mesopores on the surface. There was a reversible capacity of 180 mA h g^{-1} at a current density of 2C after 100 cycles. Zhang *et al.*[97] prepared hollow porous TiO_2 spheres with a thickness of about

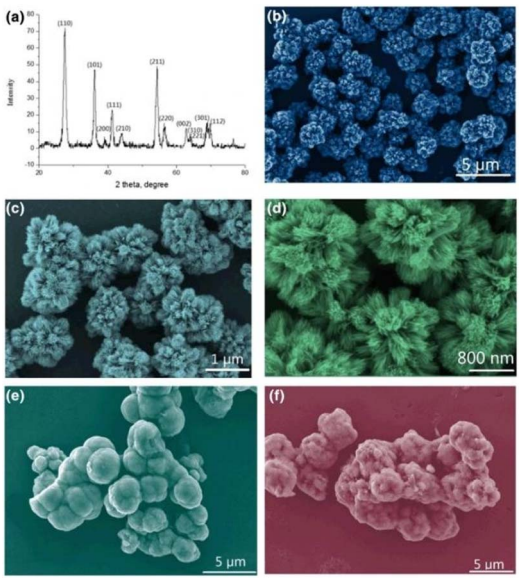

Fig. 4 XRD pattern and FE-SEM images of TiO_2 nanoflowers.[87]

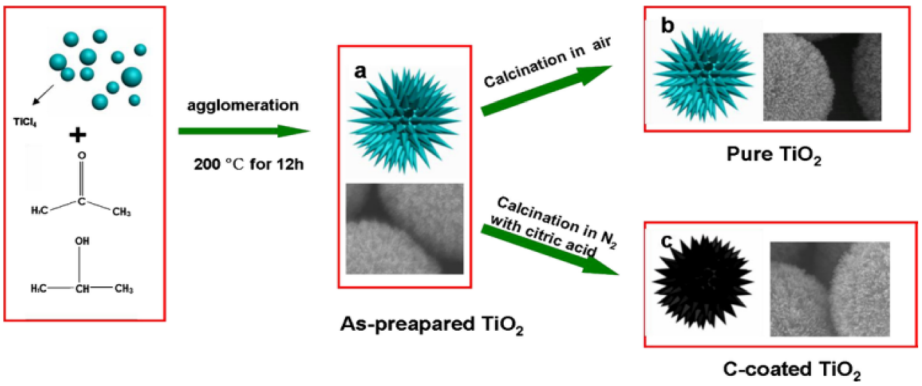

Fig. 5 Schematic diagram of the growth mechanism of TiO_2 microspheres.[94]

450 nm by hydrothermal method (see Fig. 6). This unique hollow porous structure, which facilitated the transport of Li^+, exhibited excellent electrochemical performance with a reversible capacity of 170 mA h g^{-1} at 0.6C after 150 cycles. Sunkara *et al.*[98] prepared mesoporous TiO_2 microspheres at a relatively low temperature using an acoustic-chemical synthesis method, which showed excellent cycling stability with a reversible capacity of 212.3 mA h g^{-1} after 100 charge–discharge cycles. The cycling performances and capacities of TiO_2 hollow spheres is depicted in Table 5.

TiO_2 nanotrees. TiO_2 nanotrees have the advantages of high surface area, short electron transport path, and unique morphology, which can achieve high capacity.[99–101] The structure of TiO_2 nanotrees has been less studied in recent articles, and how to construct nano-branches with ultra-thin and slender shapes to obtain a large surface area is the exploration direction for TiO_2 nanotrees in LIBs.

Wen *et al.*[99] prepared TiO_2 nanotrees by depositing ultrathin nanoribbons of mixed-phase anatase/bronzite TiO_2 on an array of single-crystal anatase nanowires. The nanotrees branches were a few nanometers thick and 200–260 nm long, and had a discharge capacity of 330 mA h cm^{-2} in the second cycle at a current density of 0.1 mA cm^{-2} with stable capacity retention over the subsequent 50 charge/discharge cycles. Sun *et al.*[100] prepared TiO_2 nanotrees composed of nanorods, nanoribbons, and nanowires nanounits by a hydrothermal method (see Fig. 7), and the shape of TiO_2 dendrimers was controlled by adjusting the precursor hydrolysis rate and surfactant. Compared with nanoparticles with smooth surfaces, the novel TiO_2 nanostructures have higher surface area and excellent electrochemical performance.

3.5 Special shape

In addition, nanostructured TiO_2 with morphologies such as microcone,[102] candied fruit, sea urchin-like, and coral-like morphologies have also been studied, which have larger surface areas due to their unique morphologies and exhibit excellent electrochemical performance. The unique morphology is difficult to control in the synthesis process, and the exploration of synthetic methods with low cost, simple operation, and adjustable morphology will become the focus of future research.

Alireza[103] synthesized coral-like TiO_2 by sol–gel method and investigated the effects of precursor hydrolysis rate, reaction time, type and concentration of acid, reaction temperature, and annealing temperature. The surface of the coral-like structure consists of nanoparticles with a cashew-like shape and a mesoporous structure with a surface area of up to 164 m^2 g^{-1}. Caruso *et al.*[104] used a polymer gel template method to obtain wall thicknesses of about 100–150 nm and coral-like TiO_2 with pore sizes ranging from 100 nm to several microns.

4 Construction of TiO_2 composites

The poor ionic and electronic conductivity of TiO_2 leads to a capacity far below the theoretical value and poor rate performance, which hinders its practical application in LIBs. Although the preparation of TiO_2 nanomaterials with a high surface area exhibits good electrochemical performance, it is still difficult to meet the commercial demand. For this reason, it is usually necessary to compound TiO_2 with other materials, and this review introduces the research progress of different types of TiO_2 composites, mainly from the compounding of TiO_2 with carbon, silicon, metals, and metal oxides.[105]

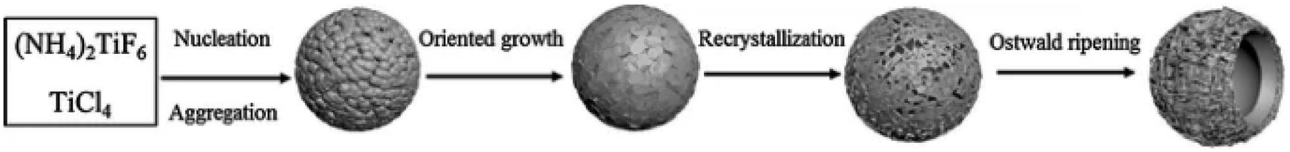

Fig. 6 Schematic illustration of the probable formation mechanism of hollow porous TiO_2 microspheres.[97]

Table 5 Cycling performances and capacities of TiO_2 hollow spheres[a]

P_m	D/nm	T/nm	S_a/m^2 g^{-1}	C_d	Initial coulombic efficiency	C_n	R_c/mA h g^{-1}	Areal capacities (mA h cm^{-2})	Ref.
T_{fm}	200–300	200	105	5C	—	800	100	0.175	89
S_m	500–2000	—	118.1	2C	—	100	180	—	96
H_m	—	450	—	0.6C	85.6%	150	170	0.24	97
S_{om}	500	—	59.4	0.25C	89%	100	212.3	0.53	98

[a] P_m—preparation method, T_{fm}—template-free method, S_m—solvothermal method, H_m—hydrothermal method, S_{om}—sonochemistry method, D—diameter, T—thickness, S_a—surface area, C_d—current density, I_{ce}—initial coulombic efficiency, C_n—cycle numbers, R_c—remaining capacity, A_c—areal capacities.

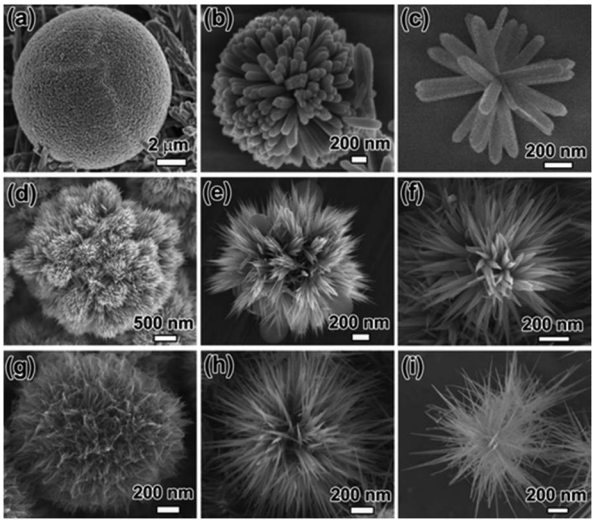

Fig. 7 SEM images of 3D nanotree composed of (a–c) nanorods (d–f) nanoribbons (g–i) nanowires.[100]

4.1 TiO_2 and carbon composite

Using the higher safety performance of TiO_2 and the excellent electrical conductivity of carbon materials, compounding TiO_2 with carbon materials is one of the development directions of TiO_2 anode materials for LIBs.[106–110] TiO_2 compounded with carbon materials such as graphene, carbon nanotubes, and hard carbon can effectively improve the electrochemical performance.[111,112] On the one hand, the introduction of carbon enhances the overall electrical conductivity of the electrode, and on the other hand, it suppresses the accumulation and agglomeration of TiO_2 nanostructures, making it easier to diffuse for Li^+ and electrons.[113]

Zhang *et al.*[114] used hollow porous pollen carbon microspheres as a backbone to load C@TiO_2 nanoparticles. C@TiO_2/3D pollen carbon (CTPC) composites with hollow porous structure were successfully prepared by a simple method (see Fig. 8). The results showed that the CTPC-700 (calcination temperature of 700 °C) composites exhibited excellent electrochemical performance with a high specific capacity of 148 mA h g^{-1} at 5C after 1000 cycles. Trang *et al.*[115] prepared a composite material consisting of mesoporous TiO_2 spheres and multi-walled carbon nanotubes by sol–gel and solvothermal methods, which exhibited excellent electrochemical performance. The first discharge capacity was 269 mA h g^{-1} at a current density of 1C, and after 100 cycles the capacity decreased by only 3.1%, with a capacity of about 260 mA h g^{-1}. Lopez *et al.*[116] synthesized a TiO_2/carbon fiber composite with first discharge and charge capacities of 683 mA h g^{-1} and 356 mA h g^{-1} at 100 mA g^{-1}, respectively, with a reversible capacity of 290 mA h g^{-1} after 100 cycles. Liang *et al.*[117] prepared two-dimensional, ultrathin and mesoporous TiO_2/reduced graphene using layer-by-layer assembly process. The synergistic effect of ultrathin mesoporous TiO_2 and reduced graphene nanosheets significantly enhanced the ion diffusion and electronic conductivity. The capacity was maintained at 245 mA h g^{-1} at 1 A g^{-1} after 1000 cycles. Mondal *et al.*[118] reported a large-scale preparation of hollow spherical TiO_2/reduced graphene composites by aerosol-assisted spray drying method. The TiO_2/reduced graphene spheres are porous and consist of 10–20 nm TiO_2 particles dispersed on the surface of reduced graphene with a surface area of 86 m^2 g^{-1}. It has good electrochemical energy storage performance with a specific capacity up to 174.4 mA h g^{-1} at a current density of 188 mA g^{-1} after 200 cycles. The cycling performances and capacities of TiO_2/C nanocomposite is depicted in Table 6.

4.2 TiO_2 and silicon composite

Silicon materials have a high theoretical capacity of 4200 mA h g^{-1} and are abundant in the earth's crust,[119] but the large bulk effect and low electrical conductivity lead to considerable challenges in related research. Silicon materials undergo structural damage during charge/discharge, resulting in lower reversible capacity, poor cycling stability, and rate performance. Although TiO_2 has minimal volume change during charge/discharge, the theoretical capacity is low at 335 mA h g^{-1}, which can be increased by compounding with silicon materials.[120]

Fang *et al.*[121] prepared a silicon–titanium core–shell structure consisting of silicon nanoparticles encapsulated in TiO_2 hollow spheres using hydrolysis and magnesium thermal reduction (see Fig. 9), which maintained a capacity of 804 mA h g^{-1} after 100 cycles at 0.1C. This excellent cycling stability and high capacity can be attributed to the unique core–shell nanostructure and the synergistic effect between silicon and TiO_2. Li *et al.*[122] coated TiO_2 on the surface of silicon nanoparticles by sol–gel method and maintained a reversible capacity of 1010.7 mA h g^{-1} after 100 cycles at a current rate of 0.1C.

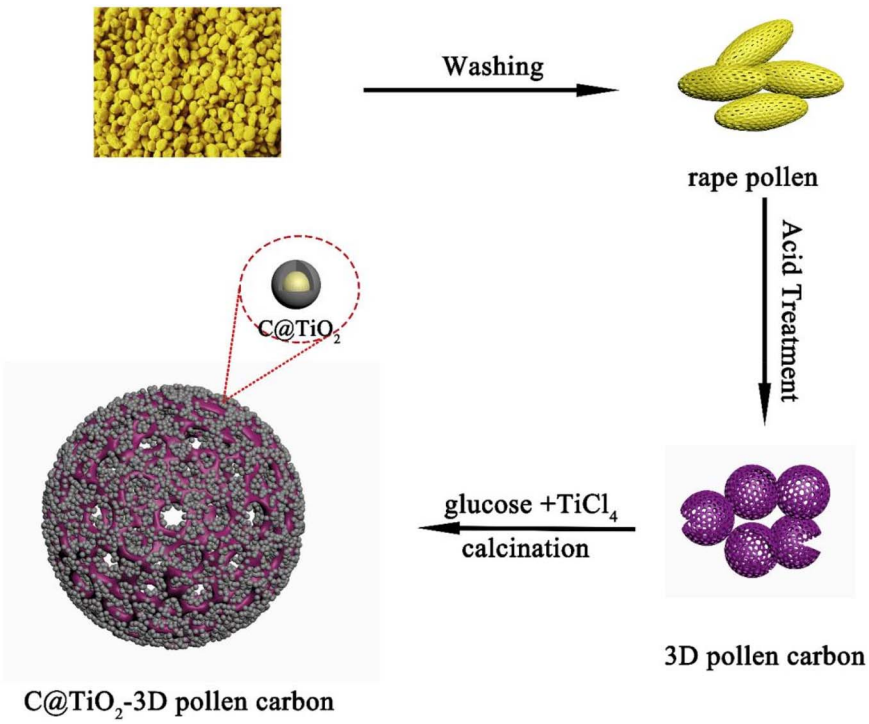

Fig. 8 Schematical illustration of the synthetic process of C@TiO_2/3D pollen carbon.[114]

Table 6 Cycling performances and capacities of TiO_2/C nanocomposite[a]

C_d	C_n	R_c/mA h g^{-1}	T_c/v	Ref.
1C	500	200	0.01–3	111
5C	1000	148	1–3	114
1C	100	269	0–3	115
100 mA g^{-1}	100	290	0.01–3	116
1 A g^{-1}	1000	245	0.01–3	117
188 mA g^{-1}	200	174.4	1–3	118

[a] C_d—current density, C_n—cycle numbers, R_c—remaining capacity, T_c—tested condition.

Excellent stability can be obtained at high current densities. Jia *et al.*[123] prepared layered nanofiber TiO_2/silica composites using natural cellulose material as a template, and their electrochemical performance improved with increasing titanium content in the composites. For composites with 54.3 wt% TiO_2 and TiO_2 nanoparticles of size 12 nm, at 200 mA g^{-1} current density, it has a capacity of 498.9 mA g^{-1} after 200 charge/discharge cycles. Zhou *et al.*[124] prepared spherical TiO_2/silica nanoparticles using the sol–gel method. It was shown that the optimal mass ratio of TiO_2/silica was 1 : 0.15, the reversible capacity was 720.9 mA h g^{-1} at a current density of 100 mA g^{-1}, and the capacity retention was 86.5% after 400 cycles, with a capacity of about 615.9 mA h g^{-1}. Yan *et al.*[125] successfully coated nano-Si with different contents of nano-TiO_2 to form a new structure of pineapple. When the molar ratio of Si/TiO_2 is 1 : 4, the cycle stability is the best. After 50 cycles at 0.1C, the specific capacity is 593 mA h g^{-1}. The cycling performances and capacities of TiO_2/Si nanocomposites is depicted in Table 7.

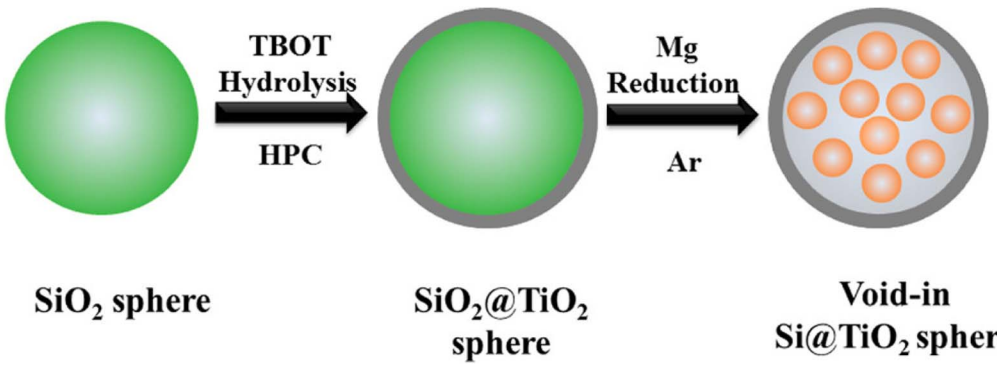

Fig. 9 Schematic diagram of the preparation process of Si@TiO_2 composite.[121]

Table 7 Cycling performances and capacities of TiO_2/Si nanocomposites[a]

C_d	Initial coulombic efficiency	C_n	R_c/mA h g^{-1}	Areal capacities (mA h cm^{-2})	T_c/v	Ref.
0.1C	53.1%	100	804	—	0.01–2.5	121
0.1C	—	100	1010.7	—	0–3	122
200 mA g^{-1}	61.5%	200	498.9	0.65	0.01–3	123
100 mA g^{-1}	67.7%	400	615.9	0.86	0.01–3	124
0.1C	69.7%	50	593	—	0–3	125

[a] C_d—current density, I_{ce}—initial coulombic efficiency, C_n—cycle numbers, R_c—remaining capacity, A_c—areal capacities, T_c—tested condition.

4.3 TiO_2 and metal element/metal oxide composite

Using the good electrical conductivity of metals to enhance the capacity and cycling stability of electrodes is a common modification method for TiO_2.[126] In recent years, there have been many reports on the compounding of TiO_2 with metal materials such as Ag, Cu, Fe, *etc.*, and metal oxides such as SnO_2,[127] Sb_2O_3, ZnO, *etc.* to improve the electrochemical performance of the materials.

Kacica *et al.*[128] prepared tin dioxide composites with a TiO_2 coating using the aerosol chemical vapor deposition method, and the SnO_2/TiO_2 electrode had a capacity of 497 mA h g^{-1} after 100 cycles at 2C current density. Compared to pure TiO_2 materials, composite SnO_2/TiO_2 composites with highly oriented, nanostructured structures exhibited better performance. Fan *et al.*[129] synthesized Cu-doped TiO_2 nano hollow spheres with a capacity of 159.06 mA h g^{-1} at a high current density of 10C after 500 cycles. Ren *et al.*[130] synthesized Ti^{3+} doped TiO_2 nanoparticles with relatively uniform particles with an average size of 30 nm and a Ti^{3+} doping content of 4 wt%, with a capacity of 145.8 mA h g^{-1} at a current density of 200 mA g^{-1} after 50 cycles. Han *et al.*[131] prepared Sb_2O_3/Sb@TiO_2 composites with TiO_2 films covering the surface of Sb_2O_3 and Sb elemental particles that were discontinuously distributed in the TiO_2 film at a discharge capacity of 609 mA h g^{-1} could be achieved at a current density of 100 mA g^{-1}. Gao *et al.*[132] reported the preparation of porous $Li_4Ti_5O_{12}$ (LTO)–TiO_2 nanosheet arrays by hydrothermal method, which had a high initial discharge capacity of 184.6 mA h g^{-1} at 200 mA g^{-1} and only lost 8.3% of the specific capacity after 1000 cycles. Cao *et al.*[133] prepared a thin layer of titanium dioxide by calcination of $MnCO_3$ microspheres and thermal decomposition of tetrabutyl titanate, and prepared a layered structure MnO_2/TiO_2 composite (nano-MnO_2@TiO_2). After 200 cycles at 300 mA g^{-1}, its capacity is 938 mA h g^{-1}. Opra *et al.*[134] synthesized vanadium-doped TiO_2-B/anatase nanotubes by a simple one-step hydrothermal reaction. The material has a mesoporous structure with a specific surface area of 179.1 m^2 g^{-1}. After 100 cycles at 3000 mA g^{-1}, the specific capacity is 133 mA h^{-1}, which has good cyclability. The cycling performances and capacities of TiO_2/metal and TiO_2/metal oxide nanocomposites is depicted in Table 8.

5 Summary and outlook

TiO_2 is a promising anode material for LIBs, but its large-scale application is limited due to its poor electrical conductivity and low Li^+ diffusion coefficient. In view of these problems, this paper reviews the research achievements of researchers to improve the electrochemical performance of TiO_2 and promote their practical applications, including the preparation of nanomaterials with different morphologies and the preparation of composite materials with other materials. Although considerable progress has been made in improving the lithium storage performance of TiO_2, there are still some fundamental issues that need to be addressed. For example, nanomaterials usually have a larger surface area, which leads to more pronounced side reactions, resulting in low coulombic efficiencies. In addition, TiO_2 nanomaterials combining with other materials is the development direction of TiO_2 anode materials, but the current preparation methods are complicated. As a result, low yields and high costs limit its commercial application. It is necessary

Table 8 Cycling performances and capacities of TiO_2/metal and TiO_2/metal oxide nanocomposites[a]

T_m	C_d	Initial coulombic efficiency	C_n	R_c/mA h g^{-1}	Areal capacities (mA h cm^{-2})	T_c/v	Ref.
SnO_2/TiO_2	2C	—	100	497	—	0.05–1.5	128
Cu/TiO_2	10C	90%	500	159.06	—	0.01–3	129
Ti^{3+}/TiO_2	200 mA g^{-1}	—	50	145.8	0.15	1–3	130
Sb_2O_3/Sb@TiO_2	100 mA g^{-1}	68.4%	500	485	—	0.01–3	131
Li $_4Ti_5O_{12}$–TiO_2	200 mA g^{-1}	—	100	172.4	—	1–3	132
MnO_2@TiO_2	300 mA g^{-1}	86%	200	938	—	0.01–3	133
V-doped TiO_2-B/anatase	3 A g^{-1}	75%	100	133	0.33	1–3	134

[a] T_m—typical materials, C_d—current density, I_{ce}—initial coulombic efficiency, C_n—cycle numbers, R_c—remaining capacity, A_c—areal capacities, T_c—tested condition.

to develop efficient and low-cost preparation methods. In conclusion, the exploration of TiO_2 anode materials with the advantages of low cost, large capacity and good cycling performance will be the focus of future research.

Conflicts of interest

There are no conflicts to declare.

Acknowledgements

This work was financially supported by the National Natural Science Foundation of China (51764008, 51864012), the Natural Science Research Project of Education Department of Guizhou Province (No. QJJ[2022]001), the Science and Technology Plan of Guizhou Province (Qian Kehe [2021]-305).

Notes and references

1 H. S. Liu, Z. H. Bi, X.-G. Sun, R. R. Unocic, M. P. Paranthaman, S. Dai and G. M. Brown, *Adv. Mater.*, 2011, **23**, 3450–3454.
2 J. S. Chen and X. W. Lou, *Small*, 2013, **9**, 1877–1893.
3 J. B. Chen, H. L. Zhao, N. Chen, X. C. Wang, J. Wang, R. Zhang and C. Q. Jin, *J. Power Sources*, 2012, **200**, 98–101.
4 S. B. Yang, X. L. Feng and K. Müllen, *Adv. Mater.*, 2011, **23**, 3575–3579.
5 S. I. Choi, E.-J. Jung, M. Park, H.-S. Shin, S. Huh and Y. S. Won, *Appl. Surf. Sci.*, 2020, **508**, 145237.
6 Q. H. Tian, D. Luo, X. W. Li, Z. X. Zhang, L. Yang and S.-I. Hirano, *J. Power Sources*, 2016, **313**, 189–197.
7 Y. Cai, H.-E. Wang, S.-Z. Huang, M. F. Yuen, H.-H. Cai, C. Wang, Y. Yu, Y. Li, W.-J. Zhang and B.-L. Su, *Electrochim. Acta*, 2016, **210**, 206–214.
8 V. Mathew, J. Gim, M. H. Alfaruqi, S. Kim, J. Song, J. P. Baboo, S. Kim, S. Park, D. Kim and J. Kim, *J. Electrochem. Soc.*, 2015, **162**, A1220–A1226.
9 Z. H. Chen, I. Belharouak, Y.-K. Sun and k. Amine, *Adv. Funct. Mater.*, 2013, **23**, 959–969.
10 D. Dambournet, I. Belharouak and K. Amine, *Chem. Mater.*, 2010, **22**, 1173–1179.
11 V. Gentili, S. Brutti, L. J. Hardwick, A. R. Armstrong, S. Panero and P. G. Bruce, *Chem. Mater.*, 2012, **24**, 4468–4476.
12 X. D. Yan, Z. H. Wang, M. He, Z. H. Hou, T. Xia, G. Liu and X. B. Chen, *Energy Technol.*, 2015, **3**, 801–814.
13 Y. Y. Zhang, Y. X. Tang, W. L. Li and X. D. Chen, *ChemNanoMat*, 2016, **2**, 764–775.
14 V. Aravindan, Y.-S. Lee, R. Yazami and S. Madhavi, *Mater. Today*, 2015, **18**, 345–351.
15 I. Ali, M. Suhail, Z. A. Alothman and A. Alwarthan, *RSC Adv.*, 2018, **8**, 30125.
16 Y. K. Tang, L. Liu, X. C. Wang, D. Z. Jia, W. Xia, Z. B. Zhao and J. S. Qiu, *J. Power Sources*, 2016, **319**, 227–234.
17 Wahyudiono, H. Kondo, M. Yamada, N. Takada, S. Machmudah, H. Kanda and M. Goto, *ACS Omega*, 2020, **5**, 5443–5451.
18 C. M. Guo, Q. H. Tian and L. Yang, *J. Alloys Compd.*, 2019, **776**, 740–745.
19 T. P. B. Rajakaruna, C. P. Udawatte, R. Chandrajith and R. M. G. Rajapakse, *ACS Omega*, 2020, **5**, 16176–16182.
20 Q. Qian, Y. Lin, Z. L. Xiong, P. H. Su, D. X. Liao, Q. Z. Dai, L. S. Chen and D. L. Feng, *Electrochem. Commun.*, 2022, **135**, 107201.
21 S. Pervez, D. Kim, C.-H. Doh, U. Farooq, A. Yaqub, J.-H. Choi, Y.-J. Lee and M. Saleem, *Mater. Lett.*, 2014, **137**, 347–350.
22 Y. X. Tang, Y. Y. Zhang, J. Y. Deng, J. Q. Wei, H. L. Tam, B. K. Chandran, Z. L. Dong, Z. Chen and X. D. Chen, *Adv. Mater.*, 2014, **26**, 6111–6118.
23 A. R. Armstrong, G. Armstrong, J. Canales and P. G. Bruce, *Angew. Chem., Int. Ed.*, 2004, **43**, 2336–2338.
24 H. Bo, Y. Yong, X. Wang and C. Ge, *ACS Appl. Mater. Interfaces*, 2013, **5**, 6285–6291.
25 W. Zhang, W. D. Zhou, J. H. Wright, Y. N. Kim, D. Liu and X. C. Xiao, *ACS Appl. Mater. Interfaces*, 2014, **6**, 7292–7300.
26 A. G. Dylla, P. H. Xiao, G. Henkelman and K. J. Stevenson, *J. Phys. Chem. Lett.*, 2012, **3**, 2015–2019.
27 Y. J. Ren, G. Q. Zhang, J. H. Huo, J. H. Li, Y. Liu and S. W. Guo, *J. Alloys Compd.*, 2022, **902**, 163730.
28 W. Dong, H. X. Li, J. H. Xi, J. X. Mu, Y. W. Huang, Z. G. Ji and X. Wu, *J. Alloys Compd.*, 2017, **724**, 280–286.
29 H. Huang, Z. Y. Yu, W. J. Zhu, Y. P. Gan, Y. Xia, X. Y. Tao and W. K. Zhang, *J. Phys. Chem. Solids*, 2014, **75**, 619–623.
30 J. B. Chen, Y. W. Wang, X. M. He, S. M. Xu, M. Fang, X. Zhao and Y. M. Shang, *Electrochim. Acta*, 2014, **142**, 152–156.
31 Z. L. Liu, L. Hong and B. Guo, *J. Power Sources*, 2005, **143**, 231–235.
32 D. K. Muthee and B. F. Dejene, *Mater. Sci. Semicond. Process.*, 2020, **106**, 104783.
33 T. Y. Peng, D. Zhao, K. Dai, W. Shi and K. Hirao, *J. Phys. Chem. B*, 2005, **109**, 4947–4952.
34 A. Mezni, N. B. Saber, M. M. Ibrahim, M. El-Kemary, A. Aldalbahi, P. Feng, L. S. Smiri and T. Altalhi, *New J. Chem.*, 2017, **41**, 5021–5027.
35 D. M. Bao and Q. H. Tian, *Chem. Phys. Lett.*, 2018, **709**, 125–129.
36 P. Mathumba, A. T. Kuvarega, L. N. Dlamini and S. P. Malinga, *Mater. Lett.*, 2017, **195**, 172–177.
37 G. Y. Huang, S. M. Xu, Z. H. Xu, H. Y. Sun and L. Y. Li, *ACS Appl. Mater. Interfaces*, 2014, **6**, 21325–21334.
38 T. Partheeban, T. Kesavan, A. Jithin, S. Dharaneshwar and M. Sasidharan, *J. Solid State Electrochem.*, 2021, **25**, 919–926.
39 W. F. Zhang, D. L. Shen, Z. W. Liu, N.-L. Wu and M. D. Wei, *Chem. Commun.*, 2018, **54**, 11491–11494.
40 K. E. Ouardi, M. Dahbi, C. Hakim, M. O. Güler, H. Akbulut, A. E. Bouari and I. Saadoune, *J. Appl. Electrochem.*, 2020, **50**, 583–595.
41 B. Zhao, F. Chen, H. Q. Liu and J. L. Zhang, *J. Phys. Chem. Solids*, 2011, **72**, 201–206.
42 H. Yin, G. Q. Ding, B. Gao, F. Q. Huang, X. M. Xie and M. H. Jiang, *Mater. Res. Bull.*, 2012, **47**, 3124–3128.

43 M. Rodríguez-Reyes and H. J. Dorantes-Rosales, *J. Sol-Gel Sci. Technol.*, 2011, **59**, 658–661.
44 E. C. Giraud, P. Mokarian-Tabari, D. T. W. Toolan, T. Arnold, A. J. Smith, J. R. Howse, P. D. Topham and M. A. Morris, *ACS Appl. Nano Mater.*, 2018, **1**, 3426–3434.
45 Y. F. Wang, M. Y. Wu and W. F. Zhang, *Electrochim. Acta*, 2008, **53**, 7863–7868.
46 F. X. Wu, X. H. Li, Z. X. Wang, H. J. Guo, L. Wu, X. H. Xiong and X. J. Wang, *Mater. Lett.*, 2011, **65**, 1514–1517.
47 H. E. Wang, Z. G. Lu, L. J. Xi, R. G. Ma, C. D. Wang, J. A. Zapien and I. Bello, *ACS Appl. Mater. Interfaces*, 2012, **4**, 1608–1613.
48 R. Govindaraj, N. Santhosh, M. Senthil Pandian and P. Ramasamy, *J. Cryst. Growth*, 2017, **468**, 125–128.
49 Q. S. Zhang, *J. Dispersion Sci. Technol.*, 2010, **31**, 1358–1361.
50 J. Jin, S.-Z. Huang, J. Shu, H.-E. Wang, Y. Li, Y. Yu, L.-H. Chen, B.-J. Wang and B.-L. Su, *Nano Energy*, 2015, **16**, 339–349.
51 X. P. Huang and C. X. Pan, *J. Cryst. Growth*, 2007, **306**, 117–122.
52 G. A. Seisenbaeva, J.-M. Nedelec, G. Daniel, G. Tiseanu, V. Parvulescu, V. G. Pol, L. Abrego and V. G. Kessler, *Chem.–Eur. J.*, 2013, **19**, 17439–17444.
53 Y. J. Ji, *Mater. Lett.*, 2013, **108**, 208–211.
54 K. Santhi, M. Navaneethana, S. Harish, S. Ponnusamy and C. Muthamizhchelvan, *Appl. Surf. Sci.*, 2020, **500**, 144058.
55 A. Ranjitha, N. Muthukumarasamy, M. Thambidurai, D. Velauthapillai, S. Agilan and R. Balasundaraprabhu, *Optik*, 2015, **126**, 2491–2494.
56 J.-H. Kim, K. Zhu, J. Y. Kim and A. J. Frank, *Electrochim. Acta*, 2013, **88**, 123–128.
57 M. Moazeni, H. Hajipour, M. Askari and M. Nusheh, *Mater. Res. Bull.*, 2014, **61**, 70–75.
58 F. Nasirpouri, I. Yousefi, E. Moslehifard and J.-K. Allafi, *Surf. Coat. Technol.*, 2017, **315**, 163–171.
59 X. Y. Zhao, Y. X. Zhu, Y. F. Wang, L. Zhu, L. B. Yang and Z. L. Sha, *J. Nanomater.*, 2015, **201**, 104193.
60 Z. H. Gong, Y. D. Hu, F. Gao, L. Quan, T. Liu, T. Gong and C. J. Pan, *Colloids Surf., B*, 2019, **184**, 110521.
61 J. W. Xu, C. H. Jia, B. Cao and W. F. Zhang, *Electrochim. Acta*, 2007, **52**, 8044–8047.
62 O. Fasakin, K. O. Oyedotun, M. Kebede, M. Rohwer, L. L. Roux, M. Mathe, M. A. Eleruja, E. O. B. Ajayi and N. Manyala, *Energy Rep*, 2020, **6**, 92–101.
63 Z. R. Wang, Y. L. Tong, L. Y. Dang, F. Gao and Q. Y. Lu, *Chem.–Eng.J.*, 2019, **370**, 1434–1439.
64 D. W. Liu, Y. H. Zhang, P. Xiao, B. B. Garcia, Q. F. Zhang, X. Y. Zhou, Y.-H. Jeong and G. Z. Cao, *Electrochim. Acta*, 2009, **54**, 6816–6820.
65 G. S. Zakharova, C. Jahne, A. Popa, Ch. Taschner, Th. Gemming, A. Leonhardt, B. Buchner and R. Klingeler, *J. Phys. Chem. C*, 2012, **116**, 8714–8720.
66 Y. Zhao, J. H. Yan, J. Y. Yu and B. Ding, *Macromol. Rapid Commun.*, 2022, 2200740.
67 S. Supothina, R. Rattanakam and S. Tawkaew, *J. Nanosci. Nanotechnol.*, 2012, **12**, 4998–5003.
68 Z.-J. Fan, J. Yan, T. Wei, G.-Q. Ning, L.-J. Zhi, J.-C. Liu, D.-X. Cao, G.-L. Wang and F. Wei, *ACS Nano*, 2011, **5**, 2787–2794.
69 H. Han, T. Song, J.-Y. Bae, L. F. Nazar, H. Kim and U. Paik, *Energy Environ. Sci.*, 2011, **4**, 4532–4536.
70 J. N. Wang, G. R. Yang, L. Wang, S. L. Wang, W. Yan and S. J. Ding, *J. Alloys. Compd.*, 2019, **787**, 1110–1119.
71 P. S. Kumar, V. Aravindan, J. Sundaramurthy, V. Thavasi, S. G. Mhaisalkar, S. Ramakrishna and S. Madhavi, *RSC Adv.*, 2012, **2**, 7983–7987.
72 J.-W. Jung, C.-L. Lee, S. Yu and I.-D. Kim, *J. Mater. Chem. A*, 2016, **4**, 703–750.
73 S. Lee, J. Ha, J. Choi, T. Song, J. W. Lee and U. Paik, *ACS Appl. Mater. Interfaces*, 2013, **5**, 11525–11529.
74 J. S. Cho, Y. J. Hong and Y. C. Kang, *Chem.–Eur. J.*, 2015, **21**, 11082–11087.
75 W. Zhuang, L. H. Lu, X. B. Wu, W. Jin, M. Meng, Y. D. Zhu and X. H. Lu, *Electrochem. Commun.*, 2013, **27**, 124–127.
76 W. Luo, X. L. Hu, Y. M. Sun and Y. H. Huang, *J. Mater. Chem.*, 2012, **22**, 4910–4915.
77 P. N. Zhu, Y. Z. Wu, M. V. Reddy, A. S. Nair, B. V. R. Chowdari and S. Ramakrishna, *RSC Adv.*, 2012, **2**, 531–537.
78 M.-C. Yang, Y.-Y. Lee, B. Xu, K. Powers and Y. S. Meng, *J. Power Sources*, 2012, **207**, 166–172.
79 F. Y. Li, Y. Huang, H. L. Peng, Y. Cao and Y. Niu, *Int. J. Photoenergy*, 2020, 3617312.
80 W. J. Yu, Y. M. Liu, N. Cheng, B. Cai, K. K. Kondamareddy, S. Kong, S. Xu, W. Liu and X.-Z. Zhao, *Electrochim. Acta*, 2016, **220**, 398–404.
81 S. H. Liu, H. P. Jia, L. Han, J. L. Wang, P. F. Gao, D. D. Xu, J. Yang and S. N. Che, *Adv. Mater.*, 2012, **24**, 3201–3204.
82 J. Q. Wang, X. P. Zou, J. L. Zhu, J. Cheng, X. Bai, Y. J. Yao, C. C. Chang, X. Yu, B. Y. Liu, Z. X. Zhou, G. D. Li and D. Chen, *Chem. Phys. Lett.*, 2021, **765**, 138284.
83 Z. D. Dai, X.-Z. Song, F. Tang, X. L. Kang, S. H. Liu, H. Abe, S. Ohara and Z. Q. Tan, *Micro Nano Lett.*, 2021, **16**, 313–318.
84 P. Shende, P. Kasture and R. S. Gaud, *Artif. Cells, Nanomed., Biotechnol.*, 2018, **46**, 413–422.
85 Z. H. Zhang, Z. F. Zhou, S. Nie, H. H. Wang, H. R. Peng, G. C. Li and K. Z. Chen, *J. Power Sources*, 2014, **267**, 388–393.
86 S. Pavasupree, S. Ngamsinlapasathian, Y. Suzuki and S. Yoshikawa, *Mater. Lett.*, 2007, **61**, 2973–2977.
87 X. Gao, Y. Q. Li, W. Zeng, C. F. Zhang and Y. M. Wei, *J. Mater. Sci. Mater. Electron.*, 2017, **28**, 18781–18786.
88 S. Ri, H. G. Deng, L. H. Zhou, J. Hu, H. L. Liu and Y. Hu, *Chin. J. Chem. Eng.*, 2014, **22**, 1153–1161.
89 M. M. Zhen, K. F. Li, S.-Q. Guo, H. Z. Li and B. X. Shen, *J. Alloys. Compd.*, 2021, **859**, 157761.
90 S. Yoon and A. Manthiram, *J. Phys. Chem. C*, 2011, **115**, 9410–9416.
91 H. Guo, T. T. Li, W. W. Chen, L. X. Liu, X. J. Yang, P. Wang and Y. C. Guo, *Nanoscale*, 2014, **6**, 15168–15174.
92 L. Yu, H. B. Wu and X. W. Lou, *Adv. Mater.*, 2013, **25**, 2296–2300.
93 G. Q. Zhang, H. B. Wu, T. Song, U. Paik and X. W. Lou, *Angew. Chem., Int. Ed.*, 2014, **53**, 1–5.

94 L. Gao, X. R. Li, H. Hu, G. J. Li, H. W. Li and Y. Yu, *Electrochim. Acta*, 2014, **120**, 231–239.
95 Y. X. Zhang, G. H. Li, Y. C. Wu and T. Xie, *Mater. Res. Bull.*, 2005, **40**, 1993–1999.
96 Y. Ma, G. Ji, B. Ding and J. Y. Lee, *J. Mater. Chem.*, 2012, **22**, 24380–24385.
97 P. G. Zhang, C. Y. Zhang, A. J. Xie, C. Li, J. M. Song and Y. H. Shen, *J. Mater. Sci.*, 2016, **51**, 3448–3453.
98 S. Sunkara, N. Munichandraiah, K. B. R. Varma and S. A. Shivashankar, *New J. Chem.*, 2016, **40**, 7197–7203.
99 W. Wen, J.-M. Wu, Y.-Z. Jiang, J.-Q. Bai and L.-L. Lai, *J. Mater. Chem. A*, 2016, **4**, 10593–10600.
100 Z. Q. Sun, J. H. Kim, Y. Zhao, F. Bijarbooneh, V. Malgras, Y. Lee, Y.-M. Kang and S. X. Dou, *J. Am. Chem. Soc.*, 2011, **133**, 19314–19317.
101 X.-Y. Li, L.-H. Chen, J. C. Rooke, Z. Deng, Z.-Y. Hu, S.-Z. Wang, L. Wang, Y. Li, A. Krief and B.-L. Su, *J. Colloid Interface Sci.*, 2013, **394**, 252–262.
102 O. Rhee, G. Lee and J. Choi, *ACS Appl. Mater. Interfaces*, 2016, **8**, 14558–14563.
103 A. Bahramian, *Ind. Eng. Chem. Res.*, 2013, **52**, 14837–14846.
104 R. A. Caruso, M. Giersig, F. Willig and M. Antonietti, *Langmuir*, 1998, **14**, 6333–6336.
105 G. M. Peng, R. A. Du, Q. M. Peng, S. Q. Wu and C. L. Yu, *Mater. Chem. Phys.*, 2018, **214**, 34–40.
106 L. Ding, J. X. Chen, B. H. Dong, Y. N. Xi, L. Shi, W. Liu and L. X. Cao, *Electrochim. Acta*, 2016, **200**, 97–105.
107 H. N. He, Q. M. Gan, H. Y. Wang, G.-L. Xu, X. Y. Zhang, D. Huang, F. Fu, Y. G. Tang, K. Amine and M. H. Shao, *Nano Energy*, 2018, **44**, 217–227.
108 Z. R. X. Guan, X. X. Wang, T. T. Li, Q. Z. Zhu, M. Q. Jia and B. Xu, *J. Mater. Sci. Technol.*, 2019, **35**, 1977–1981.
109 H. Liu, W. Li, D. K. Shen, D. Y. Zhao and G. X. Wang, *J. Am. Chem. Soc.*, 2015, **137**, 13161–13166.
110 Z. X. Huang, C. Zhao, R. P. Xu, Y. J. Zhou, R. P. Jia, X. W. Xu and S. J. Shi, *J. Alloys. Compd.*, 2020, **857**, 158048.
111 Z. G. Fu, R. X. Li and Z. Kan, *J. Solid State Electrochem.*, 2019, **23**, 1779–1785.
112 Z. G. Luo, S. N. Liu, Y. S. Cai, S. Li, A. Pan and S. Q. Liang, *Energy Technol.*, 2018, **6**, 759–765.
113 J. Zhang, J. F. Ni, J. Guo and B. Q. Cao, *New J. Chem.*, 2014, **38**, 3722–3728.
114 Y. F. Zhang, N. Zhang, J. Chen, T. Z. Zhang, W. Q. Ge, W. M. Zhang, G. Xie, L. P. Zhang and Y. H. He, *J. Alloys Compd.*, 2020, **815**, 152511.
115 N. T. H. Trang, Z. Ali and D. J. Kang, *ACS Appl. Mater. Interfaces*, 2015, **7**, 3676–3683.
116 J. Lopez, R. Gonzalez, J. Ayala, J. Cantu, A. Castillo, J. Parsons, J. Myers, T. P. Lodge and M. Alcoutlabi, *J. Phys. Chem. Solids*, 2020, **149**, 109795.
117 Y. R. Liang, X. Xiong, Z. J. Xu, Q. B. Xia, L. Y. Wan, R. T. Liu, G. X. Chen and S.-L. Chou, *Small*, 2020, **16**, 2000030.
118 A. Mondal, S. Maiti, K. Singha, S. Mahanty and A. B. Panda, *J. Mater. Chem. A*, 2017, **5**, 23853–23862.
119 D. Yan, Y. Bai, C. Y. Yu, X. G. Li and W. F. Zhang, *J. Alloys Compd.*, 2014, **609**, 86–92.
120 Z. Wei, R. S. Li, T. Huang and A. S. Yu, *J. Power Sources*, 2013, **238**, 165–172.
121 S. Fang, L. F. Shen, G. Y. Xu, P. Nie, J. Wang, H. Dou and X. G. Zhang, *ACS Appl. Mater. Interfaces*, 2014, **6**, 6497–6503.
122 J. Li, Y. Wang, Z. Y. Huang, K. Huang, X. Qi and J. X. Zhong, *J. Mater. Sci. Mater. Electrons.*, 2016, **27**, 12813–12819.
123 D. L. Jia, Y. H. Chen and J. G. Huang, *ChemNanoMat*, 2017, **3**, 120–129.
124 Y. Zhou, S. Liu, F. Liu, T. Gao, K. Fu, A. Dou, M. Su and Y. J. Liu, *Ionics*, 2020, **26**, 5349–5355.
125 D. Yan, Y. Bai, C. Y. Yu, X. G. Li and W. F. Zhang, *J. Alloys Compd.*, 2014, **609**, 86–92.
126 Q. C. Zhu, H. Hu, G. J. Li, C. B. Zhu and Y. Yu, *Electrochim. Acta*, 2015, **156**, 252–260.
127 P. P. Zhang, S. S. Zhu, Z. S. He, K. Wang, H. Q. Fan, Y. Zhong, L. Chang, H. B. Shao, J. M. Wang, J. Q. Zhang and C.-N. Cao, *J. Alloys Compd.*, 2016, **674**, 1–8.
128 C. T. Kacica, L. Wang, T. Chadha and P. Biswas, *Energy Technol.*, 2018, **6**, 1966–1974.
129 Y. C. Fan, X. H. Chen, K. Zhang, J. Rong and X. H. Yu, *J. Alloys Compd.*, 2020, **860**, 158282.
130 Y. Q. Ren, J. P. Li and J. Yu, *Electrochim. Acta*, 2014, **138**, 41–47.
131 Q. G. Han, Y. L. Sheng, Z. W. Han, X. Li, W. Q. Zhang, Y. Li and X. Zhang, *New J. Chem.*, 2020, **44**, 13430–13438.
132 L. Gao, S. H. Li, D. K. Hang, Y. Shen and M. K. Wang, *J. Mater. Chem. A*, 2015, **3**, 10107–10113.
133 Z. G. Cao, X. Q. Chen, L. D. Xing, Y. H. Liao, M. Q. Xu, X. P. Li, X. Liu and W. S. Li, *J. Power Sources*, 2018, **379**, 174–181.
134 D. P. Opra, S. V. Gnedenkov, A. A. Sokolov, A. B. Podgorbunsky, A. Y. Ustinov, V. Y. Mayorov, V. G. Kuryavyi and S. L. Sinebryukhov, *J. Mater. Sci. Technol*, 2020, **54**, 181–189.